Penetration Effect of Penetrator Geometry and Interface Friction on Rotational Penetration Resistance

Yong Tang, S.M.ASCE[1]; and Junliang (Julian) Tao, Ph.D., A.M.ASCE[2]

[1]School of Sustainable Engineering and the Built Environment, Arizona State Univ., Tempe.
Email: ytang116@asu.edu
[2]School of Sustainable Engineering and the Built Environment, Arizona State Univ., Tempe.
Email: julian.tao@asu.edu

ABSTRACT

A previous study by the authors showed that the rotational movement of a cylindrical cone penetrator could significantly reduce penetration resistance. The effects of penetrator geometry and penetrator-particle interface friction are studied to shed light on the design of a self-burrowing robot in this study. The penetrator-granular media interactions were investigated at different scales by using the discrete element method. Generally, the penetration force on the cone increases with the penetration depth but decreases with the relative slip velocity (the ratio between the rotational velocity and the vertical velocity, v_r/v). The penetration force on the cone increases in the sequence of square, decagon, and flat-end penetrators under the same conditions due to the cross section areas. Besides, the penetration force on the cone also increases with the interface friction. Force chain network and particle trajectory visualize the rotational effect at particle-scale with different penetrator geometries. Overall, the normalized penetration force on the cone decreases dramatically at first and then gradually with the increase of the relative slip velocity. The normalized penetration force on the cone for flat-end penetrator is higher than that for square and decagon penetrators under same relative slip velocity. The normalized penetration force on the cone decreases further with the increase of the interface friction under the same relative slip velocity.

INTRODUCTION

The seeds of Erodium cicutarium and Pelargonium can bury themselves into the ground for future germination by periodically repeating the coiling and uncoiling motion of the awn (Evangelista et al. 2011). The hygroscopically contracting inner layer and stiffer outer layer (Abraham and Elbaum 2013) of the awn generate the differential deformation when the humidity changes, which results in the rotational movement.

The self-burial capability of the awn was investigated through different experiments by different researchers (Jung et al. 2017). Especially, Jung et al. (Jung et al. 2017) found that the granular drag of the rotating intruder increases with the increasing penetration depth but decreases with the rotational velocity. They hypothesized that the reduction of the penetration resistance is due to the rearrangement of the grains near the intruder, which will influence the force chain network. A previous numerical study by the authors (Tang and Tao 2022) found the same results as (Jung et al. 2017). The force chain network hypothesis was validated by visualizing the force chain network between the control case and rotational cases. The authors also found that the reduction of the penetration force is related to the magnitude of the contact force, the number of particles that contact the penetrator, and the orientation of the contact forces.

The same organisms may have different geometries, which results in different burrowing mechanisms. For instance, the worm lizards have several types of heads (Gans 1968). Geometry plays an important role in burrowing. The previous numerical study by the authors modeled the geometry of the awn as a cylinder. But it is challenging to have a perfect round shape without increasing the segments number of the penetrators in DEM. Meanwhile, the cylindrical shape of the penetrator is also approximated by multiple segments in rapid prototyping when using the 3D printing technique. It would be better to directly study the geometry effect of the penetrator on the burrowing process.

Different organisms have different surface textures, which results in different interface friction between the organisms and the surrounding substrates. Snakes can double the frictional coefficient by actuating their ventral scales when moving through the narrow crevices or climbing the slopes (Marvi et al. 2016). Earthworm generates epidermal mucus to reduce the drag force when it moves inside the moist or adhesive soil (Zhang et al. 2016). Similarly, the root cap of the plant can secrete the mucilage to decrease the interface friction during the penetration process (Sadeghi et al. 2014).

The effects of geometry of the penetrator and the interface friction between the penetrator and particles were investigated using the discrete element method. The cone penetration force, force chain networks, and the trajectory of the particles were analyzed to demonstrate the effect of geometry on the reduction of the cone penetration force. Besides, the effect of interface friction on the reduction of the cone penetration force was also evaluated to shed on the design of the self-burrowing robots.

METHODOLOGY

The soil sample for the DEM simulation was prepared by using the same method as mentioned in (Tang and Tao 2022). The final dimensions of the sample were 0.4 m x 0.4 m x 0.31 m with a relative density of 0.3, as shown in Fig. 1 (a). The geometries of the penetrators (square, decagon, flat-end) were shown in Fig. 1 (b), (c), and (d). The apex angle for the square and decagon penetrator is the same, which is 60°. The cross section of these three penetrators were also shown in the figure, which has the same circumscribed circle with a diameter of 0.025 m, as shown in Fig. 1 (c). The tip length of the square and decagon penetrator is the same, which is 0.021m. Besides, the total length for all penetrators is 0.171 m. The geometrical characteristics, including n_p (shaft-diameter-to-average particle diameter ratio), R_d (diameter of container-to-shaft diameter ratio), and n_h (container height-to-shaft diameter ratio) are in the reasonable ranges(Arroyo et al. 2011), which are 5, 16, and 12.4, respectively. The open-source software YADE (Smilauer et al. 2021) was used to study the soil-penetrator interactions in this study. The soil particles were simplified as spherical balls. The built-in linear elastic-plastic model and rolling effect are considered here. Detailed information of the model construction can be found in (Tang and Tao 2022).

The microscale parameters for the numerical DEM simulation were the same as in (Tang and Tao 2022), which can also be found in Table 1. The vertical penetration velocity is 0.04 m/s for all cases, while the rotational velocities are 40, 100, 200, 400, and 600 rpm. The interface friction angles between the entire penetrator and the soil particles were set to 1.5°, and 9.5° to further investigate the effect of interface friction on the reduction of the rotational penetration resistance. The interface friction angles were chosen to simulate the smooth and rough interfaces based on that the interparticle friction angle is 19.5°. There will be no pore water pressure effect and particle breakage effect in this study, since the numerical simulation is in the dry and shallow conditions.

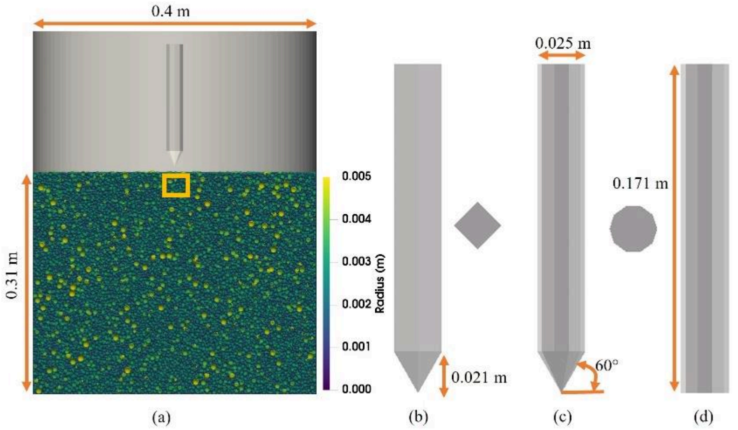

Fig. 1. The schematic diagram of the sample and penetrators: (a) numerical simulation sample; (b) square penetrator; (c) decagon penetrator; (c) flat-end penetrator (The color in Fig. 1 (a) denotes the radius of the particles; decagon indicates that the cross section of the penetrator is a ten-sided polygon; the gold square box in Fig. 1 (a) indicates the position of the measurement box, which is used to measure the trajectories of the particles.)

Table 1. Key sample and microscale parameters for the numerical sample

Parameters	Values
Sample height (mm)	310
Sample diameter (mm)	400
Relative density (D_r)	0.3
Particle density (kg/m^3)	2648
Acceleration of gravity (m/s^2)	9.81
Interparticle friction angle(°)	19.5
Penetrator–particle friction angle (°)	1.5, 9.5, 19.5
Young’s modulus (MPa)	400
Ratio of shear to normal stiffness (α_s)	0.3
Plastic moment coefficient (η)	0.5
Rolling stiffness coefficient (β)	0.2

RESULTS

Effects of cross-section area and tip end type. The penetration forces on the cone and shaft for different penetrator geometries are shown in Fig. 2. Generally, the penetration force on the cone, $\mathbf{Q_c}$, increases with the increasing penetration depth but decreases with the rotational velocities, as shown in Fig. 2 (a), (c), and (e). The $\mathbf{Q_c}$ for the decagon and square penetrators are comparable with each other due to the conical shape of the penetrators, while the $\mathbf{Q_c}$ for the flat-end penetrator is nearly 3 times of the $\mathbf{Q_c}$ for the square and decagon penetrators, while some studies showed that the cone penetration resistances for the flat-ended pile were around 2 times of the cone tip piles (Liu et al. 2020; Sheng et al. 2005). The penetration force on the shaft, $\mathbf{Q_s}$, also decreases slightly with the increase of the rotational velocities, Fig. 2 (b), (d), and (f), while the difference of the $\mathbf{Q_s}$ between any two neighboring rotational velocities is not obvious. The penetration force on the shaft is relatively small, which is only 5% of the $\mathbf{Q_c}$ for the penetrators. This might be related to the shallow penetration depth. The soil around the shaft is fully disturbed by cone tip. The soil is already in critical state, so the geometry effect on $\mathbf{Q_s}$ is not obvious at shallow depth.

The decrease of the penetration force on the cone can be visualized through the force chain networks. The force chain networks were plotted through contact normal force, the thickness of the force chain is related to the magnitude of the contact normal force. The force chain networks around the penetrators at the final penetration depth between the control case and rotational case (600 rpm) are shown in Fig. 3. The force chains for the control cases (Fig. 3 (a), Fig. 3 (b), Fig. 3 (c)) are stronger and denser than that for the rotational cases (Fig. 3 (d), Fig. 3 (e), Fig. 3 (f)) for all penetrators. Besides, the force chain networks for the square penetrator are comparable with that for the decagon penetrator, while they are significantly smaller than that for the flat-end penetrator.

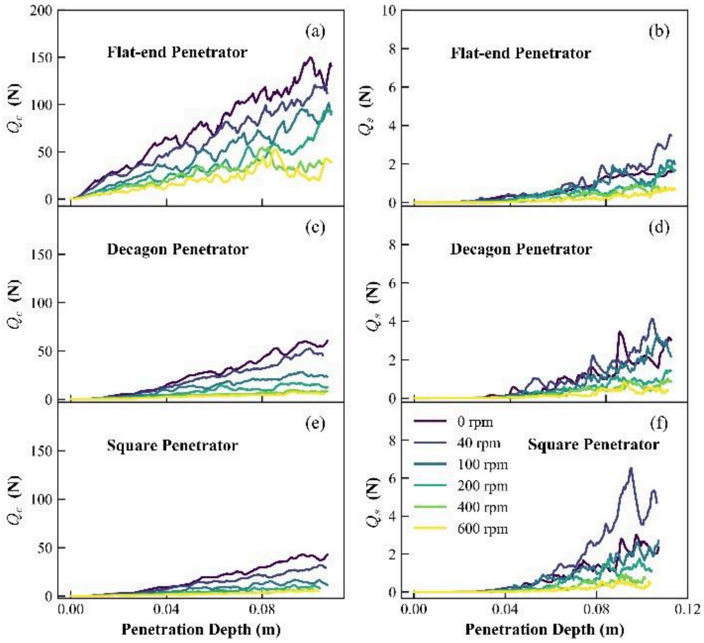

Fig. 2. Penetration force for different penetrator geometries under different rotational velocities: (a) and (b) are the penetration force on flat-end penetrator; (c) and (d) are the penetration force on decagon penetrator; (e) and (f) are the penetration force on square penetrator. (Q_c denotes the penetration force on the cone, while Q_s indicates the penetration force on the shaft.)

The trajectories of the particles inside the measurement box are shown in Fig. 4. The particles travel downward and sideways for all the control cases. However, the particles travel in a helical shape for the rotational cases. For the control cases, the particles travel further to the downward and lateral directions in the sequence of the square, decagon, and flat-end cases. The particles travel more in the horizontal plane than in the vertical plane for the rotational cases. The helical shapes were not the same for different penetrator geometries and tip end types. Different penetrator geometries make the contact particles travel in different directions, which results in different directions of the contact normal and shear force. The summation of the vertical components of the contact normal and shear force, namely, the penetration force on the cone, were also changed. However, more quantitative analysis should be further conducted to differentiate the geometry effect.

The normalized cone penetration force $(Q_{c-rot}/Q_{c-static})$ with different penetrator geometries are shown in Fig. 5. It shows that the normalized cone penetration force decreases significantly at first and then gently with the increase of the relative slip velocity for all the geometry cases. The normalized cone penetration force on the square penetrator is slightly smaller than that on the decagon penetrator when the relative slip velocity is less than 15. The normalized cone penetration force for the flat-end penetrator is larger than that for the square and decagon cases after the relative slip velocity is larger than 5.

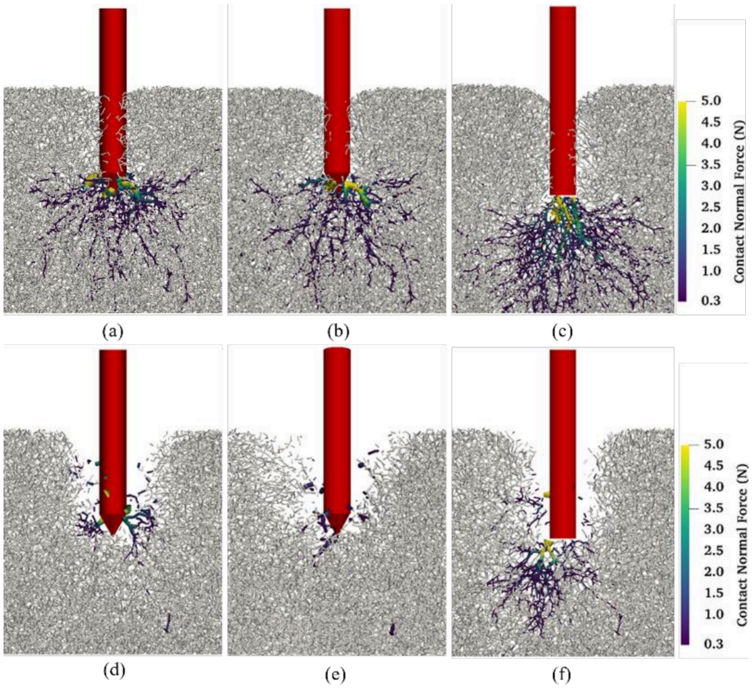

Fig. 3. Force chain networks around the penetrators at the final stage under different rotational velocities: (a) square - 0 rpm; (b) decagon - 0 rpm; (c) flat-end - 0 rpm; (d) square - 600 rpm; (e) decagon - 600 rpm; (f) flat-end - 600 rpm. (The color indicates the magnitude of the contact normal force; contact normal forces smaller than the average value (0.3 N) are represented by the gray color.)

Effects of Interface Friction. The penetration forces on the cone and shaft for decagon penetrator with different interface friction angles are shown in Fig. 6. The $\mathbf{Q_c}$ increases with the interface friction but decreases with the rotational velocity, as shown in Fig. 6 (a), (c) and (e). The $\mathbf{Q_s}$ also increases slightly with the increase of the interface friction angle, but the $\mathbf{Q_s}$ is less than 10% of the $\mathbf{Q_c}$ for all the interface friction angle cases.

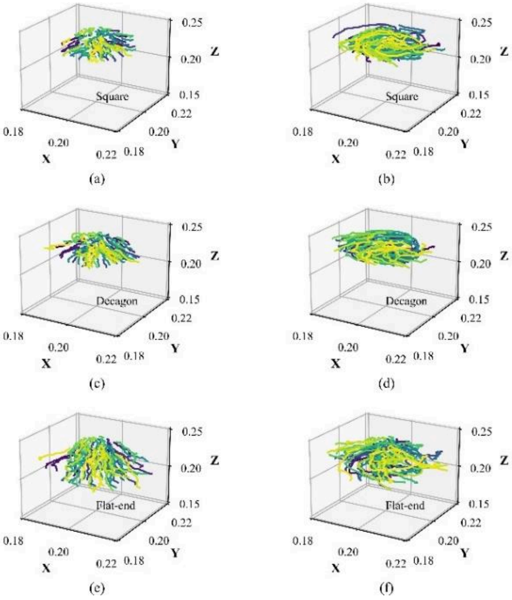

Fig. 4. Trajectories of the particles inside the measurement box: (a) square penetrator - 0 rpm; (b) square penetrator - 600 rpm; (c) decagon penetrator - 0 rpm; (d) decagon penetrator - 600 rpm; (e) flat-end penetrator - 0 rpm; (f) flat-end penetrator - 600 rpm (The color is used to differentiate different particles.)

The normalized cone penetration force ($\mathrm{Q_{c-rot}/Q_{c-static}}$) with different interface friction angles is shown in Fig. 7. It decreases with the increase of the interface friction angle under the same relative slip velocity. Besides, the difference between the $\mathrm{Q_{c-rot}/Q_{c-static}}$ under any two neighboring interface friction increases with the increase of the relative slip velocity.

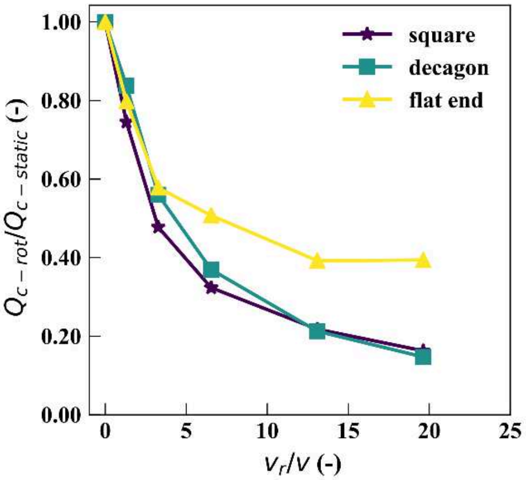

Fig. 5. Relationship between the normalized cone penetration force and relative slip velocity with different penetrator geometries (Q_{c-rot} denotes the penetration force on the cone for the rotational cases, while $Q_{c-static}$ indicates the penetration force on the cone for the control case. This notation also applies to Fig. 7.)

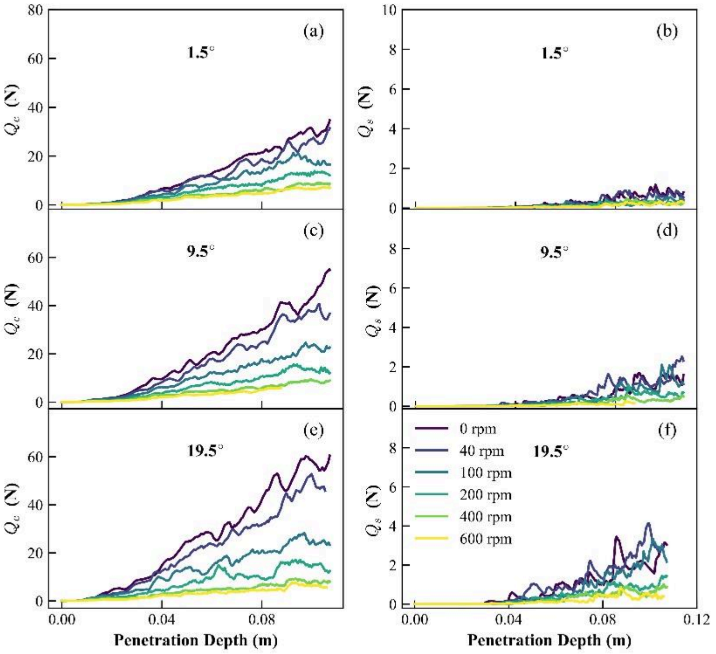

Fig. 6. Penetration force on the cone and shaft for decagon penetrator with different interface friction angles: (a) and (b) with interface friction angle = 1.5°; (c) and (d) with interface friction angle = 9.5°; (e) and (f) with interface friction angle = 19.5°.

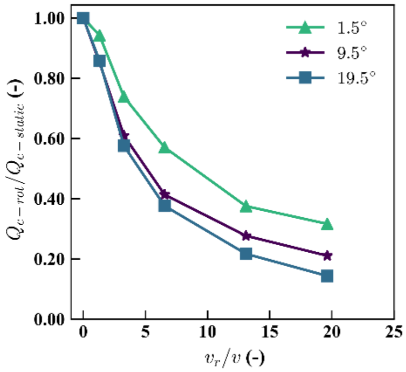

Fig. 7. Relationship between the normalized cone penetration force and relative slip velocity for the decagon penetrator with different interface friction angles.

DISCUSSIONS

The results from Fig. 2 and Fig. 5 show that the flat-end penetrator not only increases the absolute magnitude of the Q_c but also the normalized cone penetration force comparing to the square and decagon penetrator, which indicates that the penetrator with a conical shape would help the burrowing process of the robot. The reduction of the cone penetration force approaches 80% when the relative slip velocity is 20. A smaller apex angle could definitely reduce the cone penetration force (Hunt 2021), while whether a smaller apex angle could result in a higher reduction of the cone penetration force under the rotational motion should be further investigated. A higher interface friction could definitely increase the penetration force on the cone, as shown in Fig. 6. However, a higher interface friction can further decrease the normalized cone penetration force when compared with the lower interface friction under the same relative slip velocity. The cone penetration forces under a higher rotational velocity (400 rpm, 600 rpm) were comparable to each other under different interface friction angles. The penetration force on the cone consists of the normal force and friction. The result indicates that the reduction of the cone penetration force with a perfectly smooth penetrator could achieve 60% at most with the relative slip velocity is 20. Overall, it would be better to set a higher interface friction angle and have a conical tip shape for the self-burrowing robot to further reduce the resistance during the burrowing process.

CONCLUSIONS

The effects of penetrator geometry and interface friction on the reduction of the penetration force were investigated by using the discrete element method. The penetration force on the cone, Q_c, increases in the order of square, decagon, and flat-end penetrator under the same penetration depth and rotational velocity. Besides, Q_c also increases with the interface friction angle. The decreases of the penetration force on three types of penetrators can be visualized through the force chain network and particle trajectory. The normalized penetration force on the cone for the square and decagon penetrators reduces more when compared with that for the flat-end penetrator under the higher relative slip velocities. The normalized penetration force on the cone decreases with the increase of the interface friction angle under the same relative slip velocity. The results indicate that a conical shape and a higher interface friction angle will further increase the reduction of the normalized penetration force.

The rotational motion can also be applied to the offshore foundation's installation, while the geometries of the penetrator in this are still simpler than the geometries of the spudcans and anchors. This needs more comprehensive investigations.

ACKNOWLEDGEMENT

This material is based upon work supported by the National Science Foundation (NSF) under NSF CMMI 1849674 and CMMI 1841574. Any opinions, findings, and conclusions or recommendations expressed in this material are those of the authors and do not necessarily reflect those of the NSF.

REFERENCES

Abraham, Y., and R. Elbaum. 2013. "Hygroscopic movements in Geraniaceae: The structural variations that are responsible for coiling or bending." *New Phytologist*, 199 (2): 584–594.

Arroyo, M., J. Butlanska, A. Gens, F. Calvetti, and M. Jamiolkowski. 2011. "Cone penetration tests in a virtual calibration chamber." *Géotechnique*, 61 (6): 525–531.

Evangelista, D., S. Hotton, and J. Dumais. 2011. "The mechanics of explosive dispersal and self-burial in the seeds of the filaree, *Erodium Cicutarium* (Geraniaceae)." *Journal of Experimental Biology*, 214 (4): 521–529.

Gans, C. 1968. "Relative Success of Divergent Pathways in Amphisbaenian Specialization." *The American Naturalist*, 102 (926): 345–362. The University of Chicago Press.

Hunt, O. M. 2021. *Bio-Inspired Methods for Reduction of Penetration Resistance in Granular Materials*. M.{{S}}. United States – California: University of California, Davis.

Jung, W., S. M. Choi, W. Kim, and H.-Y. Kim. 2017. "Reduction of granular drag inspired by self-burrowing rotary seeds." *Physics of Fluids*, 29 (4): 041702.

Liu, C., X. Tang, H. Wei, P. Wang, and H. Zhao. 2020. "Model Tests of Jacked-Pile Penetration into Sand Using Transparent Soil and Incremental Particle Image Velocimetry." *KSCE Journal of Civil Engineering*, 24 (4): 1128–1145.

Marvi, H., J. P. Cook, J. L. Streator, and D. L. Hu. 2016. "Snakes move their scales to increase friction." *Biotribology*, 5: 52–60.

Sadeghi, A., A. Tonazzini, L. Popova, and B. Mazzolai. 2014. "A Novel Growing Device Inspired by Plant Root Soil Penetration Behaviors." *PLoS ONE*, (J. Bongard, ed.), 9 (2): e90139.

Sheng, D., K. D. Eigenbrod, and P. Wriggers. 2005. "Finite element analysis of pile installation using large-slip frictional contact." *Computers and Geotechnics*, 32 (1): 17–26.

Smilauer, V., et al. 2021. "Yade documentation." Zenodo.

Tang, Y., and J. Tao. 2022. "Multiscale analysis of rotational penetration in shallow dry sand and implications for self-burrowing robot design." *Acta Geotechnica*.

Zhang, D., Y. Chen, Y. Ma, L. Guo, J. Sun, and J. Tong. 2016. "Earthworm epidermal mucus: Rheological behavior reveals drag-reducing characteristics in soil." *Soil and Tillage Research*, 158: 57–66.